Effect of the Interfacial Energy Landscape on Photo-induced Charge Generation at the ZnPc-MoS_2 Interface

Tika R. Kafle[1], Bhupal Kattel[1], Peng Yao[1, 2], Peymon Zereshki[1], Hui Zhao[1], Wai-Lun Chan[1,*]

[1]Department of Physics and Astronomy, University of Kansas, Lawrence, KS 66045

[2] Key Laboratory of Luminescence and Optical Information, Ministry of education, Institute of Optoelectronic Technology, Beijing Jiaotong University, Beijing 100044, China

Abstract

Monolayer transition-metal dichalcogenide crystals (TMDC) can be combined with other functional materials, such as organic molecules, to from a wide range of heterostructures with tailorable properties. Although a number of works have shown that ultrafast charge transfer (CT) can occur at organic-TMDC interfaces, conditions that would facilitate the separation of interfacial CT excitons into free carriers remain unclear. Here, time-resolved and steady-state photoemission spectroscopy are used to study the potential energy landscape, charge transfer and exciton dynamics at the zinc phthalocyanine (ZnPc)/monolayer (ML) MoS_2 and ZnPc/bulk MoS_2 interfaces. Surprisingly, although both interfaces have a type-II band alignment and exhibit sub-100 femtosecond CT, the CT excitons formed at the two interfaces show drastically different evolution dynamics. The ZnPc/ML-MoS_2 behaves like typical donor-acceptor interfaces in which CT excitons dissociate into electron-hole pairs. On the contrary, back electron transfer occur at ZnPc/bulk-MoS_2, which results in the formation of triplet excitons in ZnPc. The difference can be explained by the different amount of band bending found in the ZnPc film deposited on ML-MoS_2 and bulk-MoS_2. Our work illustrates that the potential energy landscape near the interface plays an important role in the charge separation behavior. Therefore, considering the energy level alignment at the interface alone is not enough for predicting whether free charges can be generated effectively from an interface.

INTRODUCTION

Layered two-dimensional (2D) materials such as transition metal dichalcogenide crystals (TMDCs) have attracted much attention recently because they allow materials properties to be tailored by stacking different atomically thin crystals together.[1-3] This "stackability" is enabled by the weak van der Waals (vdW) bonding between layers and the absence of dangling bonds at the interface. Similar to TMDCs, organic molecules are bonded together by vdW forces. Hence, organic molecules can be combined readily with TMDCs to produce heterostructures that possess advantages of both materials.[4-7] For instance, organic molecules are excellent light absorbers and the thickness of an organic film can be controlled easily. They can be combined with TMDCs, which have outstanding and gate-tunable carrier mobility, to produce sensitive detectors and gate-tunable p-n junctions.[8-14] More excitingly, the hybrid system can realize new properties and functionalities that neither materials can provide. For example, atomically-thin lateral[15] and vertical p-n junctions[16] can be fabricated in a scalable fashion by doping TMDCs with organic molecules. Combining organic molecules with other layered materials such as Bi_2Se_3 can create exotic systems such as lateral topological p-n junctions.[17,18] Moreover, organic molecules can passivate defects in TMDCs *via* either physical[19] or chemical adsorption,[20,21] which is important for improving the carrier mobility in TMDCs. Technically, large area organic-TMDC heterostructures can be synthesized readily in a scalable fashion.

Recent works have shown that femtosecond (fs) to picosecond (ps) charge transfer (CT) can occur across some organic-TMDC interfaces.[22-27] However, CT across the interface is only the first step for generating free carriers from bound excitons. The CT process will likely produce Coulombic-bound electron-hole pairs at the interface (commonly known as CT excitons or indirect excitons).[28] The relaxation and dissociation mechanisms of these CT excitons at the interface are

not well-understood. In most applications, it is desired that these CT excitons can dissociate effectively into free electron-hole pairs. However, other competing electronic processes would occur prior to the exciton dissociation. In fact, the separation of CT excitons into free carriers is known to be a process that would limit the performance of organic photovoltaics[29,30] and possibly optoelectronic devices made with other excitonic materials. Therefore, identifying conditions that would favor effective exciton dissociation is of paramount importance for fabricating effective devices based on organic-TMDC heterostructures.

Although a type-II band alignment generally enables effective CT across the interface, the subsequent evolution of the CT exciton, which plays an important role in the generation of free charges, is a more complicated process that depends critically on the potential energy landscape near the interface. Unfortunately, very few works directly measure both the energy landscape near the interface and the evolution dynamics of the CT exciton. Without knowing the correlation between the two at the molecular level, designing interfaces for effective exciton dissociation remains a trial-and-error task. Here, by using zinc phthalocyanine (ZnPc)/MoS_2 interface as a prototype system, we illustrate the importance of the band bending, in addition to the interfacial energy level alignment, on the spatial range of coherent CT and the evolution of the CT exciton. In particular, we compare the exciton dynamics at ZnPc/monolayer (ML)-MoS_2 and ZnPc/bulk-MoS_2 interfaces. Surprisingly, the two seemingly similar interfaces show distinctly different charge separation behaviors. Although both interfaces has a type-II band alignment, our photoemission spectroscopy measurement shows that the two possess different amount of band bending in the ZnPc film near the interface. Because of the differences in the band bending and the spin lifetime in ML-MoS_2 and bulk-MoS_2,[31,32] CT excitons at the ZnPc/bulk-MoS_2 interface recombine to form triplet (T_1) exciton *via* back electron transfer, while CT excitons at the

ZnPc/ML-MoS_2 interface can separate into free carriers. Despite both interfaces exhibit sub-100 fs CT, the very different evolution dynamics of the CT exciton implies that the two interfaces can be suitable for different applications. For instance, the ZnPc/bulk-MoS_2 interface can be used for triplet sensitization,[33] while the ZnPc/ML-MoS_2 interface can be used for effective charge separation.

EXPERIMENTAL METHODS

Sample Preparation. Commercially available, high quality, CVD-grown ML-MoS_2 on SiO_2/Si (6Carbon Technology, Shenzhen) was used. The ML-MoS_2 layer has a continuous coverage and a microscopy image of these samples is shown in the supporting information (Fig. S1). For bulk-MoS_2, a cm-sized single crystal purchased from SPI supplies was used. Before the measurement, the MoS_2 samples were annealed at 400°C for 12 hours in an ultrahigh vacuum chamber (UHV) with a base pressure of 1×10^{-10} Torr. The quality of our bulk-MoS_2 sample was reported previously in Ref. [24]. For the ML-MoS_2 sample, angle-resolved photoemission spectroscopy (ARPES) was used to characterize the band structure of the material. A clear band-structure was observed in the ARPES experiment (supporting information, Fig. S2), indicating that the ML-MoS_2 has a continuous coverage, good crystallinity and a clean surface. The valence band (VB) edge at the K point is located at a slightly higher energy than the VB edge at the Γ point, which is a characteristic feature of ML-MoS_2.[34,35] The ML-MoS_2 has a photoluminescence (PL) peak at ~ 660 nm (supporting information, Fig. S3), which is consistent to the properties of ML-MoS_2.[36] Furthermore, the CVD-grown ML-MoS_2 has an exciton decay dynamics that is comparable to that of a mechanically exfoliated ML-MoS_2 sample obtained from a bulk-MoS_2 crystal (supporting information, Fig. S4).

After the bare MoS_2 surface was annealed, it was then transferred *in-situ* to another UHV chamber with a base pressure of 1×10^{-9} Torr for ZnPc deposition. The nominal thickness of the ZnPc film was monitored by a quartz crystal microbalance. The uncertainty in the nominal thickness measured by this method was ~ 5 - 10 %, which was mainly originated from the uncertainty in determining the mass density of the film. A film density of 1.55 g cm^{-3} was used to calculate the film thickness. For thicknesses up to 4 nm, a substrate temperature of 90 °C and a deposition rate of 0.3 Å/min were used. These conditions are known to produce a uniform ZnPc

film with molecules having a face-on orientation.[37] The ZnPc orientation can be verified using ultraviolet photoemission spectroscopy (UPS)[38,39] and we found that ZnPc molecules in our films have a face-on orientation (supporting information, Fig. S5). For film thicknesses larger than 4 nm, a faster deposition rate of 0.8 Å/min was used and the sample was kept at room temperature. After ZnPc deposition, the sample was transferred back to the photoemission chamber where the photoemission experiments were performed.

ARPES and UPS Spectroscopy. In the UPS and ARPES measurements, UV light generated from a standard UV lamp was used to ionize electrons from the sample. The He-I emission line with a photon energy of 21.22 eV was used. The energy and the emission angle of photoelectrons were measured using a hemispherical analyzer equipped with an imaging detector (Phoibos 100, SPECS).

Time-resolved Two Photon Photoemission (TR-TPPE) Spectroscopy. TR-TPPE spectroscopy was used to measure the excited state dynamics of the sample. The details of the TR-TPPE setup can be found in our previous publication.[40] In short, the TR-TPPE is a pump-probe spectroscopy technique in which the energy and population of excited electrons were measured by using photoemission spectroscopy. In this work, the pump and probe beam have a photon energy of 1.77 eV and 4.68 eV respectively. The pump and probe beams were generated by using the outputs of two non-collinear optical parametric amplifiers (NOPA), which were pumped by a Yb:KGW regenerative amplifier running at 125 kHz (Pharos, 10 W, Light Conversion). The pump and probe beams have a pulse duration of 25 fs and 65 fs respectively. The beams have a Gaussian profile with a full width half maxima (fwhm) size of ~ 0.8 mm. The kinetic energy of the photoelectrons ionized by the probe beam was measured by the aforementioned hemispherical electron analyzer. The measurement was done at room temperature.

Transient Absorption Measurement. In the transient absorption measurements, an 80-MHz Ti:sapphire oscillator produces ~100 fs pulses at about 840 nm. Part of this beam was focused to a BBO crystal to generate its second harmonic at 420 nm, which is used as the probe pulse. The rest of the 840-nm beam was coupled to a photonic crystal fiber to generate a broadband supercontinuum. A bandpass filter with a bandwidth of 10 nm was used to select the 710 nm component of the supercontinuum, which serves as the pump pulse. The two pulses are combined by a beam splitter and co-focused by a microscope objective lens to the sample surface with a spot size of about 2 μm. We measured differential reflection of the probe as a function of the probe

delay. The differential reflection is defined as $\Delta R/R_0 = (R-R_0)/R_0$, where R and R_0 are the reflection coefficient of the sample at the probe wavelength. To measure this quantity, the probe beam reflected by the sample was send to a silicon photodiode, which output was detected by a lock-in amplifier. A mechanical chopper was used in the pump arm to modulate the pump intensity at about 2 kHz, for the lock-in detection. The time delay between the pump and probe pulses was controlled by changing the path length of the pump beam by using a linear stage. All measurements were performed with the sample at room temperature.

RESULTS AND DISCUSSION

Interfacial band alignment and band bending

Because the interfacial band alignment and the band bending play important roles in the CT and exciton dissociation dynamics, we will first discuss the band structure of the ZnPc/ML-MoS_2 and the ZnPc/bulk-MoS_2 interfaces measured by the UPS experiment. One of the major differences in the band structure between ML-MoS_2 and bulk-MoS_2 is that the energy of the valence band (VB) edge at the Γ point increases with the number of MoS_2 layers because of the interlayer electronic coupling.[34,41] The energy upshift, from ML to bulk, of the VB-edge at the Γ point results in the well-known transition from a direct to an indirect gap semiconductor.[36] Figure 1a compares the UPS spectra of our ML-MoS_2 and bulk-MoS_2 samples measured at the Γ point. The energy is referenced with respect to the Fermi level (E_f). The VB-edge at the Γ point of the bulk-MoS_2 is ≈ 0.65 eV higher than that of the ML-MoS_2, which agrees well with first principle calculation[34] and micro-ARPES measurement.[35] The positions of the VB-edges with respect to the E_f for ML- and bulk-MoS_2 are shown in Fig. 1b. We further note that both samples have similar workfunctions (ML: 4.55 eV; bulk: 4.65 eV). Hence, a similar energy upshift in the VB-edges can be obtained if the energy is referenced with respect to the vacuum level. For bulk-MoS_2, the VB-edge at the Γ point is the valence band maxima (VBM). For the ML-MoS_2 sample, we found that

the band edge at the Γ point is slightly lower than that at the K point, which is consistent with previous theoretical and experimental works.[34,35,41] The angle-resolved spectra are shown in the Fig. S2 in the supporting information. Figure 1b summarizes the key differences between the band-structure of our ML and bulk MoS_2 samples. Positions of the conduction band minimum (CBM) are assigned based on reported transport gaps of ML and bulk MoS_2.[34,42]

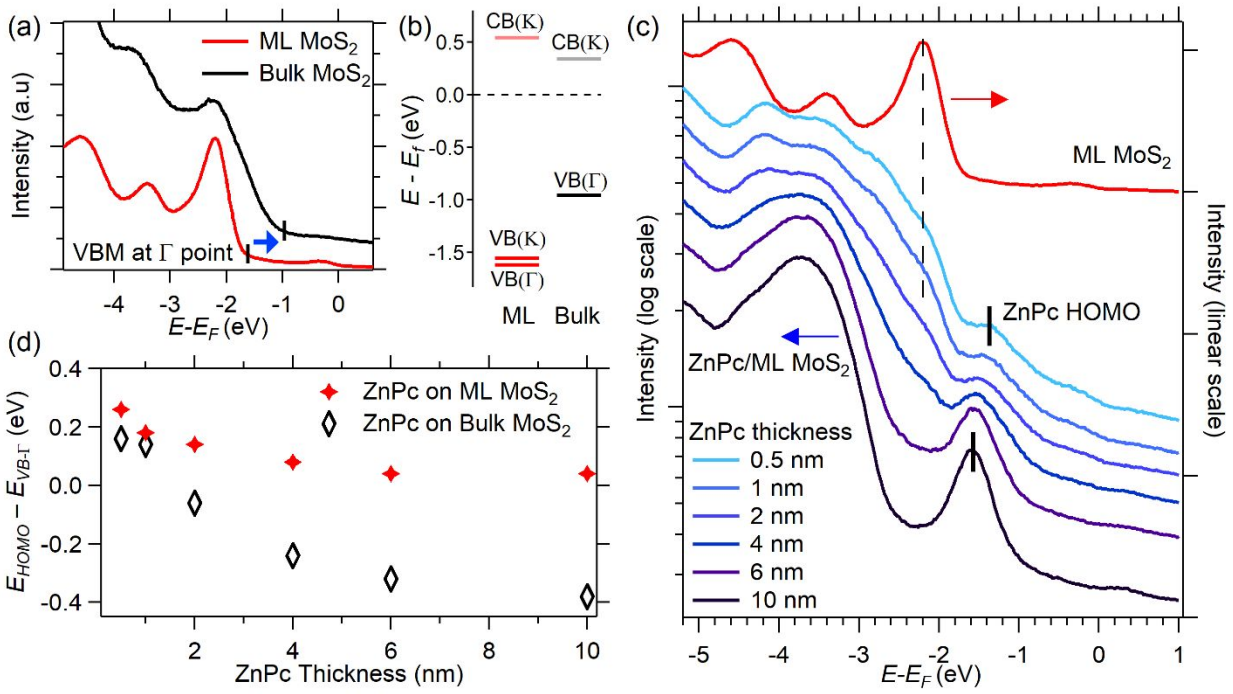

Figure 1: (a) The UPS spectra for ML and bulk MoS_2 at the Γ point. The VB-edges are indicated by the vertical bars. (b) A comparison between the band structure of ML and bulk MoS_2. (c) The UPS spectra for ZnPc/ML-MoS_2 with various ZnPc's thickness. The position of the ZnPc's HOMO peak is indicated be the vertical bars. For comparison, the spectrum for the ML-MoS_2 is also shown (red line). The spectra for the ZnPc/ML-MoS_2 samples are plotted in a log scale such that features from both layers can show up clearly in the 0.5 nm and 1 nm spectra.(d) The HOMO-VB edge offset at ZnPc/ML-MoS_2 and ZnPc/bulk-MoS_2 interfaces as a function of the ZnPc's thickness.

If all the energy levels are aligned using a common vacuum level, one would anticipate that the energy offsets between the MoS_2's VB-edge and the ZnPc's HOMO would be very different for the ZnPc/ML-MoS_2 and the ZnPc/bulk MoS_2 interfaces. This is because the energy of the VBM of ML and bulk MoS differs by ≈ 0.6 eV (Fig. 1b). However, surprisingly, a very

similar energy offset (in the range of 0.2 - 0.3 eV) is observed for both interfaces (ZnPc/ML-MoS_2, ZnPc/bulk-MoS_2). Figure 1c shows the UPS spectra of the ML-MoS_2 sample with various ZnPc thicknesses as ZnPc molecules are deposited consecutively on the MoS_2 surface. The ZnPc's HOMO peaks (vertical bars) can be identified for a nominal thickness as small as 0.5 nm. For comparison, the spectrum for the bare ML-MoS_2 is also shown (red line). The first major peak in the MoS_2 valence band (dashed line) is still visible in the ZnPc/MoS_2 spectra for small ZnPc thicknesses. The offset between the ZnPc's HOMO and the MoS_2's VB-edge at the Γ-point is 0.26 eV. With an increase in the ZnPc thickness, the HOMO peak shifts to a slightly lower energy (i.e. a larger binding energy). The energy offset ($E_{HOMO} - E_{VB\text{-}\Gamma}$) as a function of ZnPc thickness is plotted in Fig. 1d. For comparison, we have also included the energy offset for the ZnPc/bulk-MoS_2 interface that are reported in our pervious study.[24]

Two important observations stem from the above comparison. First, for small ZnPc thicknesses (0.5 – 1 nm), both interfaces show a very similar energy offset. As mentioned earlier, this is rather surprising because the energy of the VB-edge at the Γ point for ML MoS_2 is significantly lower than that for bulk MoS_2 (Fig. 1b). The physical origin of this observed "pinning" in the VB-HOMO offset is not clear, but we speculate that it would be resulted from the orbital mixing between MoS_2 and ZnPc considering that the MoS_2 orbit at the Γ-point has a strong out-of-plane character.[34] Based on this offset, both ZnPc/ML-MoS_2, ZnPc/ bulk-MoS_2 interfaces have a type-II band alignment. The type-II band alignment is consistent with other reports on the metal-Pc/ML-MoS_2 interface.[27,43-45] Second, there is a much stronger band bending in the ZnPc film deposited on bulk-MoS_2 than on ML-MoS_2. It is known that ZnPc molecules on MoS_2 have a face-on orientation.[46] For this orientation, our previous studies[47] found that the position of the HOMO peak is in the range of 1.2 - 1.5 eV below the E_f and the workfunction is in the range of

4.3 - 4.5 eV. Comparing these numbers with the VB-edge position of the bulk-MoS_2 (Fig. 1b), one can find that if the energy offset between ZnPc's HOMO and MoS_2's VB-edge is pinned at ~0.2 - 0.3 eV, the E_f of ZnPc would be much higher than that of bulk-MoS_2. Thus, ground state electron transfer from ZnPc to bulk-MoS_2 needs to occur in order to produce the observed energy level alignment. The expected ground state electron transfer is indeed consistent with the strong band bending observed in ZnPc deposited on bulk-MoS_2. The direction of the band bending indicates that net positive charges are accumulated in the ZnPc layer.[48] The different amount of the band bending for ZnPc/ML-MoS_2 and ZnPc/bulk-MoS_2 interfaces should have a strong influence on the CT and the subsequent evolution of the CT states.

Charge Transfer Excitons at the ZnPc/ML-MoS_2 interface

The ZnPc/ML-MoS_2 interface has a type-II band alignment, which should allow ultrafast electron transfer from ZnPc to ML-MoS_2. Figure 2a shows the TR-TPPE spectrum of a 1 nm ZnPc/ML-MoS_2 sample. In the TR-TPPE experiment, the sample is excited by a 1.77 eV pump beam. This photon energy is enough to excite the S_1 state of ZnPc,[49] but it is below the optical band gap of the ML-MoS_2.[36] One of the unique advantages of the TR-TPPE spectroscopy is that it measures the energy of excited states directly. On the vertical axis in Fig. 2a, the energy of excited states is referenced with respect to the ZnPc's HOMO position determined from our UPS experiment. The pseudocolor represents the pump-induced photoemission intensity. At delay time $t \approx 0$ ps, a peak at ≈ 1.75 eV is observed. Figure 2b shows the spectra at various delay times and the peak at $E - E_{HOMO} \approx 1.75$ eV is apparent in the 0.01 ps and 0.03 ps spectra. We attribute this peak to the S_1 state of ZnPc because the peak position agrees well with the energy of the S_1 exciton. Note that it cannot be originated from excitons in ML-MoS_2 because in a control experiment conducted on the bare MoS_2 sample, we observe negligible TR-TPPE signal (supporting

information, Fig. S6). This is reasonable because the pump photon energy is less than the bandgap of ML-MoS_2. This S_1 state decays rapidly on a sub-100 fs timescale (Fig. 2c, open squares). The decay of the S_1 population can be attributed to the electron transfer from ZnPc to MoS_2.[24,50] In our TR-TPPE setup, the pump-probe cross-correlation has a fwhm width of 70 fs (Fig. 2c, solid black line). Fitting the S_1 decay to a single exponential decay convoluted with the widths of the pump and probe pulses yields a CT time of 40 fs (dashed line).

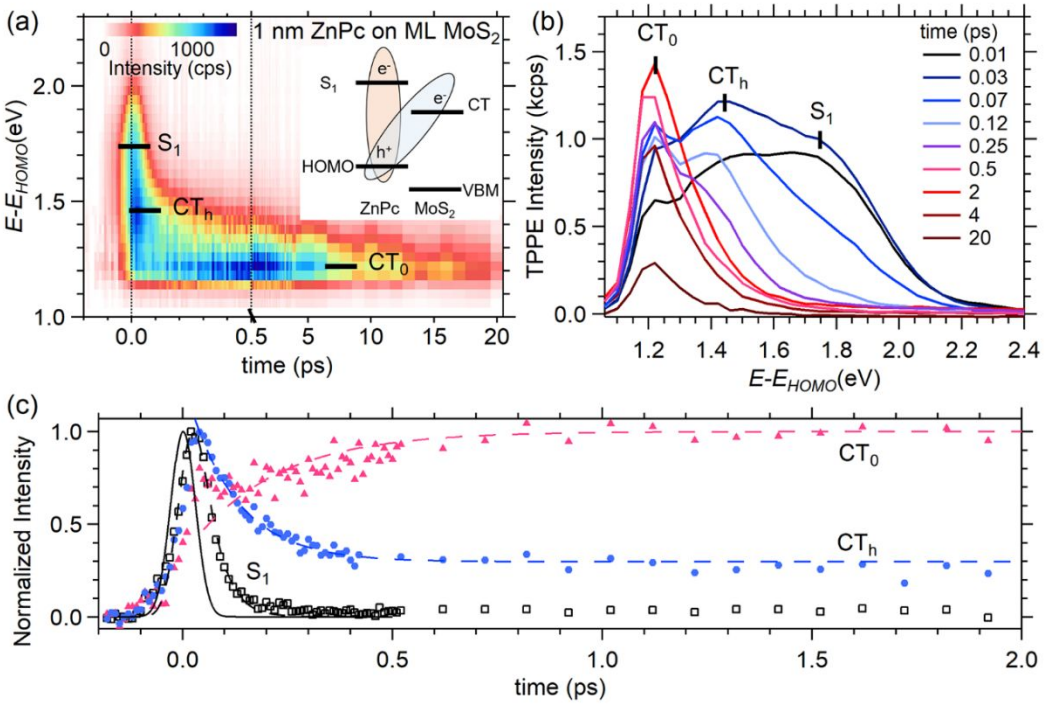

Figure 2: (a) TR-TPPE spectrum of the 1 nm-ZnPc/ML-MoS_2 sample. The pump beam excites the ZnPc film selectively and the interfacial CT exciton is produced by electron transfer from ZnPc to MoS_2. The time axis is split at 0.5 ps in order to show the dynamics on two different timescales. The inset is a schematic diagram showing the energy level alignment at the interface, ZnPc's S_1 exciton and CT excitons. (b) TPPE spectra at some selected pump-probe delay times. The positions for the S_1, CT_h and CT_0 states are shown. (c) The intensity of the S_1, CT_h and CT_0 states as a function of time. The solid black line shows the pump-probe cross-correlation. The lifetime of the S_1 state is fit by a rate equation model that accounts for the pulse width of pump and probe pulses (black dashed line). The blue and red dashed line are fits to single exponential decay and single exponential rise respectively.

Another peak located at ≈ 0.2 eV below the S_1 peak can be found in the spectrum. This state has a slightly delayed intensity rise (Fig. 2c, solid circle) and a longer lifetime as compared

to the S_1 peak. A fit to an exponential decay yields a lifetime of 120 fs (Fig 2c, blue dashed line). We assign this state to a hot charge transfer state (CT_h) that consists of a pair of Coulombic-bound electron and hole in MoS_2 and ZnPc respectively (inset in Fig. 2a). Similar CT exciton states unveiled by optical absorption spectroscopy has been reported recently for the CuPc/MoS_2 interface.[45] The CT state can be populated by the CT from ZnPc to MoS_2. The energy of this state is ≈ 1.7 eV above the MoS_2's VBM (1.44 eV with respect to the ZnPc's HOMO). This energy is slightly lower compared to the A-exciton energy of ML-MoS_2 (1.87 eV), but it is within our experimental uncertainty (~ ± 0.1 eV). In our experiment, error would be introduced in determining the relative energy position of the HOMO (in the UPS spectrum) and the excited state (in the TPPE spectrum) because different light sources used in the two experiments would introduce different sample charging conditions. The slightly lower energy of the CT exciton indicates that it would have a larger binding energy as compared to the A-exciton of MoS_2, which can be resulted from the more localized nature of the molecular orbit. Finally, a state at $E - E_{HOMO} \approx 1.22$ eV can be found, which clearly shows a delayed population rise. The rise time of this state is 200 fs (Fig. 2c, red dashed line). This state can be populated from the relaxation of the CT_h state. Following previous TR-TPPE works on other donor-acceptor interfaces,[51-53] we assign this peak to a relaxed, localized CT state (CT_0).

Moreover, we note that the probe photons (4.68 eV) used in our experiment do not have a large enough in-plane momentum to ionize excited electrons residing at the K-valleys of MoS_2 *via* a direct optical process.[54,55] However, as mentioned earlier, it is likely that the electron in these CT excitons localizes spatially and do not have a well-defined momentum vector in the *k*-space. Hence, the momentum conservation requirement for photoionization cannot be applied to this case. We will come back to this point when the lifetime of the CT_0 state is discussed.

Comparison of the coherent CT range between ZnPc/ML-MoS_2 and ZnPc/bulk-MoS_2

Previously, we have reported that sub-100 fs electron transfer from ZnPc to MoS_2 can also occur at the ZnPc/bulk-MoS_2 interface.[24] Hence, ultrafast CT can occur at both ZnPc/ML-MoS_2 and ZnPc/bulk-MoS_2 interfaces, which is consistent with the similar ZnPc-HOMO/MoS_2-VBM offset found for both interfaces. However, when the ZnPc film becomes thicker, we find that there is a subtle difference in the spatial range of the CT, i.e. the distance from the interface in which the ultrafast CT would still occur. Figure 3a and 3b show the temporal evolution of the normalized S_1 peak intensity for ZnPc/ML-MoS_2 and ZnPc/bulk MoS_2 samples with various ZnPc film thicknesses. Because photoemission is a surface sensitive technique, it mainly probes the population of excitons near the ZnPc surface. By varying the thickness of the ZnPc layer, we can estimate the distance from the interface in which the sub-100 fs CT would still occur. Previously, we have used this method to study the transport mechanism and the delocalization size of excitons in organic thin films.[40,56] For an ultrathin (0.5 nm) ZnPc layer, the S_1 peak intensity shows an ultrafast decay in both ZnPc/ML-MoS_2 and ZnPc/bulk MoS_2 samples. By fitting the data to a single exponential decay convoluted with the laser pulse widths (Fig. 3a and b, dashed lines), we found that the ZnPc's S_1 exciton has lifetimes of 40 fs and 55 fs for ZnPc/ML-MoS_2 and ZnPc/bulk MoS_2 respectively, which are attributed to the CT times.

As the ZnPc thickness is increased to 1 ~ 2 nm, the S_1 peak intensity starts to show a slower decay for the bulk-MoS_2 sample (Fig. 3b). By contrast, the decay dynamics is independent of thickness (in the range of 0.5 – 2 nm) for the ML-MoS_2 samples (Fig. 3a). Eventually, when the ZnPc thickness is beyond 4 nm, the S_1 exciton shows a much slower and thickness-independent decay for both samples. Thicker samples show a much slower decay because S_1 excitons near the ZnPc surface need to transport to the interface *via* slow incoherent diffusion before the interfacial

CT can occur.[24,50] However, if the average thickness of the film is roughly equal to or less than the delocalization size of the S_1 exciton in the ZnPc film, fast population quenching due to the coherent CT can still be observed. The results in Fig. 3a and 3b imply that the S_1 exciton in the ZnPc film deposited on the bulk-MoS_2 has a smaller delocalization size because the ultrafast quenching can no longer be observed in samples with a ZnPc layer as thin as 2 nm. The difference in the delocalization size can be correlated to the amount of band bending found in the UPS measurement (Fig. 1d). For the ZnPc/bulk-MoS_2, the amount of the band bending (~ 0.6 eV) is larger than the electronic coupling between neighboring phthalocyanine molecules (~0.1 eV).[57,58] This uneven energy landscape would limit the coherent size of the S_1 exciton. Moreover, the direction of the electric field associated with the band bending pushes the electron away from the interface. These key differences between the two interfaces are summarized schematically in Fig. 3d. For ZnPc/bulk-MoS_2, a S_1 exciton slightly farther away from the interface can no longer transfer its electron coherently to the MoS_2. On the other hand, the lesser band bending in ZnPc on ML-MoS_2 results in the larger delocalization size of the S_1 exciton, which can enable coherent CT even though the exciton is farther away from the interface. For practical applications, this larger coherent CT range is important because it will allow the interface to dissociate a larger amount of S_1 excitons on the sub-ps timescale.

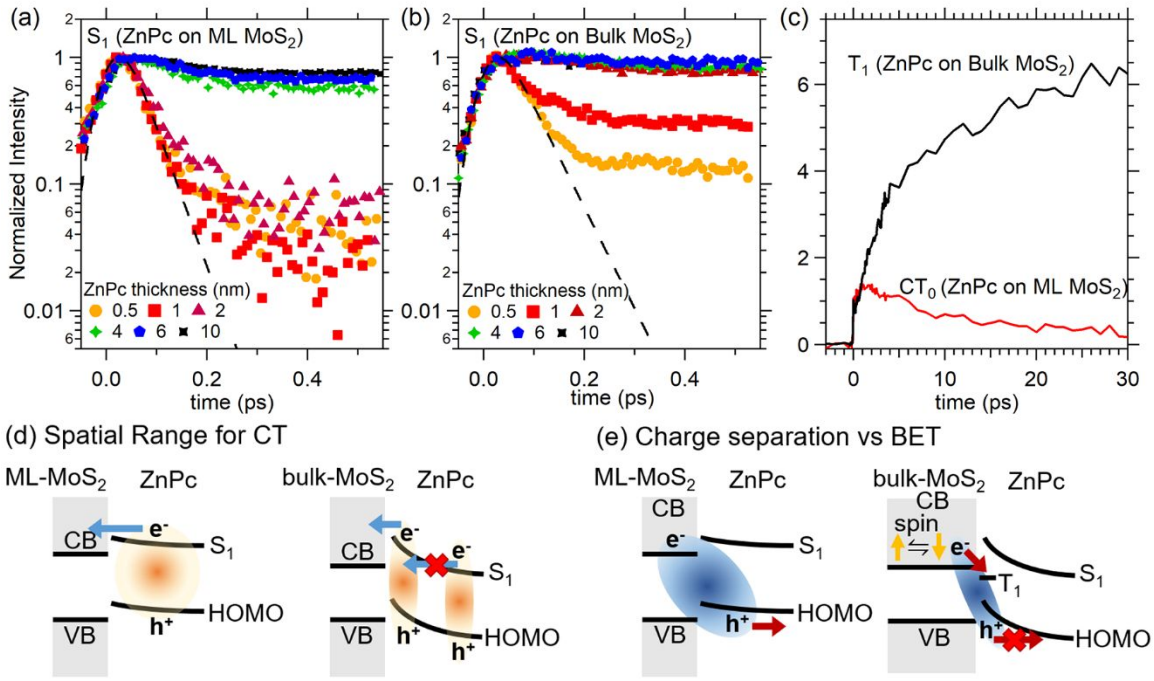

Figure 3: The S_1 peak intensity as a function of time for samples with various ZnPc thicknesses. Panel (a) and (b) show the results from the ML and bulk MoS_2 respectively. The dashed lines show the fit to an exponential decay. (c) The temporal evolution of the intensity for the CT_0 and T_1 states in the 1 nm ZnPc/ML-MoS_2 and the 1 nm ZnPc/bulk-MoS_2 samples respectively. (d) A schematic diagram shows that a large band bending in ZnPc on bulk MoS_2 can limit the extent of exciton delocalization and prohibit electron injection. These two factors limit the spatial range of the coherent CT. (e) Large band bending in ZnPc on bulk MoS_2 can trap the hole of the CT exciton near the interface. The hole trapping together with the faster spin flipping rate in bulk-MoS_2 favor back electron transfer (BET) and T_1 formation at the ZnPc/bulk-MoS_2 interface.

Competition between Back Electron Transfer and Exciton Dissociation

After the initial CT process, the CT exciton formed at the interface needs to be dissociated in order to generate free carriers. However, other electronic processes can compete with the dissociation of the CT exciton. Indeed, for bulk-MoS_2/ZnPc, we have reported that triplet (T_1) exciton can be formed in the ZnPc film *via* spin-flipping in MoS_2 and subsequent back electron transfer (BET) from bulk-MoS_2 to ZnPc.[24] For ZnPc/bulk-MoS_2, the population of the T_1 exciton was found to increase on the 10 – 100 ps timescales. The T_1 formation kinetics for 1 nm-ZnPc/bulk-MoS_2 is reproduced in Fig. 3c (the black curve). The spectral signature of the T_1 exciton is rather distinctive in the TPPE spectrum[24] because the signal intensity is larger compared to other states

and it has a very long lifetime. However, such a T_1 state is not observed for the ZnPc/ML-MoS_2 interface. The longest-lived state identifiable in the 1 nm ZnPc/ML-MoS_2 spectrum (Fig. 2) is the CT_0 state. For comparison, the intensity evolution of this state is shown in Fig. 3c (red curve). After the intensity is peaked at ~ 1 ps, it decreases monotonically with time. Hence, we do not observe the signature for the BET and T_1 formation at the ZnPc/ML-MoS_2 interface.

For the ZnPc/bulk-MoS_2 interface, two factors that favor the T_1 formation can be identified. First, the spin lifetime is supposed to be longer in ML-MoS_2 as compared to bulk-MoS_2 because of the spin-momentum locking in ML-MoS_2.[31,32] Indeed, recent works on ML-TMDC heterostructures have shown that CT excitons in these heterostructures can have a very long spin lifetime.[59] Second, the large band bending in the ZnPc film on bulk-MoS_2 can essentially trap the hole of the CT exciton very close to the interface (Fig. 3e). The close proximity of the hole in ZnPc to the electron in MoS_2 can increase the chance of the BET. Indeed, the exchange interaction that provides the energetic driving force for the T_1 formation is a very short range interaction (within the size of a molecule). Hence, hole trapping at the interface would be a crucial step for T_1 formation *via* the BET. We note that band bending has also been invoked recently to explain the triplet formation at the CuPc/GaAs interface.[60]

We do not observe significant T_1 formation at ZnPc/ML-MoS_2. Instead, the CT_0 intensity is found to decay on the order of 10s of ps (Fig. 3c). The disappearance of the CT_0 state can be explained by two different scenarios. In the first scenario, the interfacial CT exciton simply recombines at the interface. However, this seems to be unlikely because a number of recent time-resolved studies found that the CT states or separated carriers in similar organic-TMDC interfaces have much longer lifetimes.[23,25,26] In the second scenario, the localized CT exciton dissociates into an electron-hole pair with the hole in ZnPc and the electron in MoS_2. However, the signal

disappears because our TR-TPPE probe is not sensitive to both delocalized electrons in MoS_2 and holes in ZnPc. The TR-TPPE cannot probe the hole in ZnPc because it can only measure excited electrons. For separated electrons in ML-MoS_2, they are resided at K valleys in the momentum space, which has a large in-plane momentum. To detect these electrons, momentum conservation will need to be fulfilled in the photoionization process[61] (the probe process) and a probe photon energy of ~ 10 – 20 eV is required.[54,55] Our probe photons only have an energy of 4.68 eV, which is not enough to ionize electrons in the K valleys through a direct optical process. As a result, our probe is not sensitive to the separated electrons in MoS_2. Indeed, our control experiments on bare ML-MoS_2 (supporting information) shows that the TPPE signal is an order of magnitude weaker compared to the ZnPc/MoS_2 samples even when the ML-MoS_2 is excited resonantly at ≈ 1.88 eV. Similarly, in bare bulk-MoS_2, the primary photo-excited species is free electron and no TPPE signal can be observed.[24] These control experiments shows that our TPPE probe cannot detect free electrons at the K valleys in MoS_2. Therefore, the gradual decrease in the CT_0 intensity can be explained by the dissociation of localized CT excitons (which do not have a well-defined *k*-vector) into delocalized electrons in the ML-MoS_2 with a well-defined momentum.

To distinguish the above two scenarios, another time-resolved probe is used to detect long-lived excited states that may have been missed out by the TR-TPPE experiment. Transient absorption measurement is done on the 2 nm ZnPc/ML-MoS_2 sample to find out whether long-lived states exist. In this experiment, the sample is pumped at 710 nm (1.75 eV, similar to the pump wavelength used in the TPPE experiment) and the transient change in reflectance at 420 nm is measured. As mentioned above, the pump photons selectively excite ZnPc and no significant signal is observed in the bare ML-MoS_2 sample (Supporting information, Fig. S7). The choice of the probe wavelength is limited by the experimental setup. In particular, we did not choose a probe

wavelength of 660 nm (which can probe the A-exciton bleaching in MoS_2 directly) because it would be too close to the pump wavelength. Nevertheless, this probe wavelength (420 nm) can detect excitation in both ZnPc and MoS_2. In Fig. 4, the transient change in the reflectance ($\Delta R/R$) for the ZnPc/ML-MoS_2 sample is shown (solid square), which is compared to the data obtained from a 10 nm ZnPc/SiO_2/Si sample (open circle). For comparison, the signal from the ZnPc-only sample is divided by a factor of 5 to account for its larger thickness. It is clear that the positive signal in both traces is originated from the ZnPc layer, which can be attributed to the photobleaching of the ZnPc's B-band (an increase in R can be resulted from a decrease in absorption). The measured dynamics for the ZnPc-only sample is comparable to the S_1 exciton population in the same sample measured by TR-TPPE (solid line).

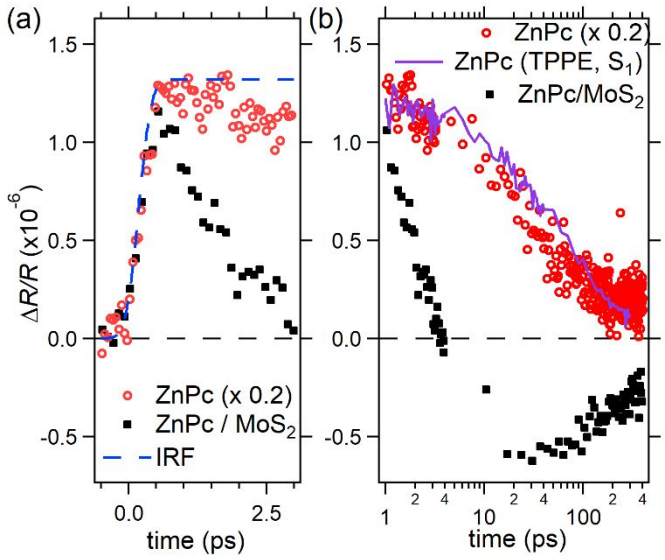

Figure 4: The transient absorption of the 2 nm ZnPc/ML-MoS_2 and 10 nm ZnPc samples measured at 420 nm. The samples are pumped at 710 nm, which selectively excites the ZnPc's S_1 exciton. For comparison, the signal for the ZnPc-only sample is divided by 5 to account for the difference in the ZnPc film thickness. Panel (a) and (b) show the dynamics on two different timescales. In panel (a), the instrumental response function (IRF), which is the integral of a Gaussian function with a fwhm of 400 fs, is indicated by the dashed line. In panel (b), the S_1 peak intensity of the ZnPc-only sample measured by the TR-TPPE experiment (solid line) is shown for comparison.

The initial signal rise overlaps with the instrumental response (~ 400 fs) indicated by the dashed line in Fig. 4a. Hence, the positive signal near time zero is originated from the optically-

excited S_1 exciton in ZnPc. For the ZnPc/ML-MoS_2 sample, the positive signal decreases rapidly in the first 1 – 2 ps, which is consistent to the annihilation of the S_1 exciton *via* ultrafast CT discussed above. Then, the signal changes to negative after a few ps, which magnitude decays on a 100 ps time scale. The decay time of the positive signal is similar to that of the CT_0 population observed in the TR-TPPE experiment (Fig. 3c). Following the decay of the positive signal, a long-lived negative signal appears at $t \sim 20$ ps. We attribute the long-lived negative signal to the population of electrons in ML-MoS_2 resulted from the dissociation of CT excitons. The probe photon energy is close to the C-exciton resonance of MoS_2.[62] Hence, the signal originates from the change of the C-exciton resonance by these electrons. The decay time of several 100 ps is also consistent with lifetime of electrons in MoS_2 when they are spatially separated from holes by a vdW interface in TMDC heterobilayers.[63,64] Unlike excitons, which reduce transient absorption of exciton resonances mainly by phase space state filling effect and thus produce photobleaching, electrons as charged particles can alter the exciton resonance effectively by screening effect, which mainly cause a shift of the resonance. Hence, the sign of the signal (photoinduced absorption or photobleaching) depends on the direction of the shift. In the measurement, we found the signal to be negative. Based on both the transient absorption and the TR-TPPE measurements, we conclude that the CT_0 exciton does not recombine. Instead, they dissociate into free electrons in MoS_2 and holes in ZnPc.

Compared to typical organic-organic interfaces, the time taken for the dissociation of the CT exciton at the ZnPc/MoS_2 interface is relatively short (~ 10 ps). For example, bound CT excitons at the ZnPc/C_{60} interface dissociate on the ~1 ns timescale.[53,65] The relatively fast CT exciton dissociation dynamics can be explained by a smaller exciton binding energy. Moreover, the delocalized nature of electrons in MoS_2 should increase the density of less-localized and

loosely bound CT states. A larger number of available CT states with small binding energies and large spatial extents should favor the CT exciton dissociation driven by the entropy.[66-68]

CONCLUSION

A major conclusion that can be drawn from our work is that although the type-II band alignment is necessary for enabling ultrafast interfacial CT, it is not a decisive factor in determining whether free electrons and holes can be generated effectively from the interface. In particular, we demonstrate that the potential energy landscape near the interface, together with the spin lifetime in the TMDC, can govern the spatial range of the coherent interfacial CT process and the subsequent evolution of the CT exciton. Both ZnPc/ML-MoS_2 and ZnPc/bulk-MoS_2 interfaces are found to have a type-II band alignment with a similar MoS_2-VBM/ZnPc-HOMO energy offset at the interface. However, the VBM of bulk-MoS_2 has a higher energy than that of the ML-MoS_2, which results in the much stronger band bending found in the ZnPc film deposited on the bulk-MoS_2. This band bending not only limits the spatial range of the coherent CT, it also determines the eventual fate of CT excitons. For ZnPc/bulk-MoS_2, CT excitons transition into triplet excitons in ZnPc *via* faster spin flipping in bulk-MoS_2 and more effective back electron transfer to ZnPc. We attribute the more effective back electron transfer process to the larger band bending in ZnPc because the hole in ZnPc is likely to be trapped at the interface by the large potential gradient associated with the band bending. By contrast, the flatter band structure at the ZnPc/ML-MoS_2 interface and the longer spin lifetime in ML-MoS_2 favor the dissociation of the CT excitons. The very different exciton dynamics found at the two interfaces shows that the interfacial energy level alignment, by itself, is not a good predictor in determining whether free charges can be generated effectively from these interfaces.

ASSOCIATED CONTENT

Supporting Information

Data on the characterization of the monolayer MoS_2, additional UPS, TR-TPPE and transient absorption data for control experiments.

AUTHOR INFORMATION

Corresponding Authors

*wlchan@ku.edu

Notes

The authors declare no competing financial interest.

ACKNOWLEDGEMENT

This work is primarily supported by the U.S. National Science Foundation, grant DMR-1351716. This investigation was also supported by the University of Kansas General Research Fund allocation #2151080. H.Z. acknowledges the support from U.S. National Science Foundation, grant DMR-1505852.

REFERENCES

(1) Novoselov, K. S.; Mishchenko, A.; Carvalho, A.; Neto, A. H. C., 2D materials and van der Waals heterostructures, *Science*, **353**, 461 (2016).
(2) Zhang, W. J.; Wang, Q. X.; Chen, Y.; Wang, Z.; Wee, A. T. S., Van der Waals stacked 2D layered materials for optoelectronics, *2D Mater.*, **3**, 022001 (2016).
(3) Das, S.; Robinson, J. A.; Dubey, M.; Terrones, H.; Terrones, M., Beyond Graphene: Progress in Novel Two-Dimensional Materials and van der Waals Solids, *Annu. Rev. Mater. Res.*, **45**, 1-27 (2015).
(4) Jariwala, D.; Marks, T. J.; Hersam, M. C., Mixed-dimensional van der Waals heterostructures, *Nat. Mater.*, **16**, 170-181 (2017).
(5) Huang, Y. L.; Zheng, Y. J.; Song, Z. B.; Chi, D. Z.; Wee, A. T. S.; Quek, S. Y., The organic-2D transition metal dichalcogenide heterointerface, *Chem. Soc. Rev.*, **47**, 3241-3264 (2018).
(6) Wang, H. M.; Li, C. H.; Fang, P. F.; Zhang, Z. L.; Zhang, J. Z., Synthesis, properties, and optoelectronic applications of two-dimensional MoS_2 and MoS_2-based heterostructures, *Chem. Soc. Rev.*, **47**, 6101-6127 (2018).
(7) Sun, J.; Choi, Y.; Choi, Y. J.; Kim, S.; Park, J.-H.; Lee, S.; Cho, J. H., 2D-Organic Hybrid Heterostructures for Optoelectronic Applications, *Adv. Mater.*, 1803831 (2019).
(8) Velez, S.; Ciudad, D.; Island, J.; Buscema, M.; Txoperena, O.; Parui, S.; Steele, G. A.; Casanova, F.; van der Zant, H. S. J.; Castellanos-Gomez, A.; Hueso, L. E., Gate-tunable diode and photovoltaic effect in an organic-2D layered material p-n junction, *Nanoscale*, **7**, 15442-15449 (2015).

(9) Liu, F. C.; Chow, W. L.; He, X. X.; Hu, P.; Zheng, S. J.; Wang, X. L.; Zhou, J. D.; Fu, Q. D.; Fu, W.; Yu, P.; Zeng, Q. S.; Fan, H. J.; Tay, B. K.; Kloc, C.; Liu, Z., Van der Waals p-n Junction Based on an Organic-Inorganic Heterostructure, *Adv. Funct. Mater.*, **25**, 5865-5871 (2015).
(10) Pak, J.; Jang, J.; Cho, K.; Kim, T. Y.; Kim, J. K.; Song, Y.; Hong, W. K.; Min, M.; Leec, H.; Lee, T., Enhancement of photodetection characteristics of MoS_2 field effect transistors using surface treatment with copper phthalocyanine, *Nanoscale*, **7**, 18780-18788 (2015).
(11) Jariwala, D.; Howell, S. L.; Chen, K. S.; Kang, J. M.; Sangwan, V. K.; Filippone, S. A.; Turrisi, R.; Marks, T. J.; Lauhon, L. J.; Hersam, M. C., Hybrid, Gate-Tunable, van der Waals p-n Heterojunctions from Pentacene and MoS_2, *Nano Lett.*, **16**, 497-503 (2016).
(12) Liu, X.; Gu, J.; Ding, K.; Fan, D. J.; Hu, X. E.; Tseng, Y. W.; Lee, Y. H.; Menon, V.; Forrest, S. R., Photoresponse of an Organic Semiconductor/Two-Dimensional Transition Metal Dichalcogenide Heterojunction, *Nano Lett.*, **17**, 3176-3181 (2017).
(13) Huang, Y.; Zhuge, F. W.; Hou, J. X.; Lv, L.; Luo, P.; Zhou, N.; Gan, L.; Zhai, T. Y., Van der Waals Coupled Organic Molecules with Monolayer MoS_2 for Fast Response Photodetectors with Gate-Tunable Responsivity, *ACS Nano*, **12**, 4062-4073 (2018).
(14) Cho, Y.; Park, J. H.; Kim, M.; Jeong, Y.; Yu, S.; Lim, J. Y.; Yi, Y.; Im, S., Impact of Organic Molecule-Induced Charge Transfer on Operating Voltage Control of Both n-MoS_2 and p-$MoTe_2$ Transistors, *Nano Lett.*, **19**, 2456-2463 (2019).
(15) Choi, M. S.; Qu, D.; Lee, D.; Liu, X.; Watanabe, K.; Taniguchi, T.; Yoo, W. J., Lateral MoS2 p-n Junction Formed by Chemical Doping for Use in High-Performance Optoelectronics, *ACS Nano*, **8**, 9332-9340 (2014).
(16) Li, H. M.; Lee, D.; Qu, D. S.; Liu, X. C.; Ryu, J. J.; Seabaugh, A.; Yoo, W. J., Ultimate thin vertical p-n junction composed of two-dimensional layered molybdenum disulfide, *Nat. Commun.*, **6**, 6564 (2015).
(17) Tu, N. H.; Tanabe, Y.; Satake, Y.; Huynh, K. K.; Tanigaki, K., In-plane topological p-n junction in the three-dimensional topological insulator $Bi_{2-x}Sb_xTe_{3-y}Se_y$, *Nat. Commun.*, **7**, 13763 (2016).
(18) Kim, S. H.; Jin, K. H.; Kho, B. W.; Park, B. G.; Liu, F.; Kim, J. S.; Yeom, H. W., Atomically Abrupt Topological p-n Junction, *ACS Nano*, **11**, 9671-9677 (2017).
(19) Park, J. H.; Sanne, A.; Guo, Y. Z.; Amani, M.; Zhang, K. H.; Movva, H. C. P.; Robinson, J. A.; Javey, A.; Robertson, J.; Banerjee, S. K.; Kummel, A. C., Defect passivation of transition metal dichalcogenides via a charge transfer van der Waals interface, *Sci. Adv.*, **3**, 1701661 (2017).
(20) Yu, Z. H.; Pan, Y. M.; Shen, Y. T.; Wang, Z. L.; Ong, Z. Y.; Xu, T.; Xin, R.; Pan, L. J.; Wang, B. G.; Sun, L. T.; Wang, J. L.; Zhang, G.; Zhang, Y. W.; Shi, Y.; Wang, X. R., Towards intrinsic charge transport in monolayer molybdenum disulfide by defect and interface engineering, *Nat. Commun.*, **5**, 5290 (2014).
(21) Li, Q.; Zhao, Y. H.; Ling, C. Y.; Yuan, S. J.; Chen, Q.; Wang, J. L., Towards a Comprehensive Understanding of the Reaction Mechanisms Between Defective MoS_2 and Thiol Molecules, *Angew Chem. Int. Ed.*, **56**, 10501-10505 (2017).
(22) Petoukhoff, C. E.; Krishna, M. B. M.; Voiry, D.; Bozkurt, I.; Deckoff-Jones, S.; Chhowalla, M.; O'Carroll, D. M.; Dani, K. M., Ultrafast Charge Transfer and Enhanced Absorption in MoS_2-Organic van der Waals Heterojunctions Using Plasmonic Metasurfaces, *ACS Nano*, **10**, 9899-9908 (2016).

(23) Homan, S. B.; Sangwan, V. K.; Balla, I.; Bergeron, H.; Weiss, E. A.; Hersam, M. C., Ultrafast Exciton Dissociation and Long-Lived Charge Separation in a Photovoltaic Pentacene-MoS_2 van der Waals Heterojunction, *Nano Lett.*, **17**, 164-169 (2017).
(24) Kafle, T. R.; Kattel, B.; Lane, S. D.; Wang, T.; Zhao, H.; Chan, W. L., Charge Transfer Exciton and Spin Flipping at Organic-Transition-Metal Dichalcogenide Interfaces, *ACS Nano*, **11**, 10184-10192 (2017).
(25) Zhong, C. M.; Sangwan, V. K.; Wang, C.; Bergeron, H.; Hersam, M. C.; Weiss, E. A., Mechanisms of Ultrafast Charge Separation in a PTB7/Monolayer MoS_2 van der Waals Heterojunction, *J. Phys. Chem. Lett.*, **9**, 2484-2491 (2018).
(26) Zhu, T.; Yuan, L.; Zhao, Y.; Zhou, M. W.; Wan, Y.; Mei, J. G.; Huang, L. B., Highly mobile charge-transfer excitons in two-dimensional WS_2/tetracene heterostructures, *Sci. Adv.*, **4**, 3104 (2018).
(27) Canton-Vitoria, R.; Gobeze, H. B.; Blas-Ferrando, V. M.; Ortiz, J.; Jang, Y.; Fernández-Lázaro, F.; Sastre-Santos, Á.; Nakanishi, Y.; Shinohara, H.; D'Souza, F.; Tagmatarchis, N., Excited-State Charge Transfer in Covalently Functionalized MoS_2 with a Zinc Phthalocyanine Donor–Acceptor Hybrid, *Angew. Chem. Int. Ed.*, **131**, 5768-5773 (2019).
(28) Zhu, X. Y.; Monahan, N. R.; Gong, Z. Z.; Zhu, H. M.; Williams, K. W.; Nelson, C. A., Charge Transfer Excitons at van der Waals Interfaces, *J. Am. Chem. Soc.*, **137**, 8313-8320 (2015).
(29) Yao, J. Z.; Kirchartz, T.; Vezie, M. S.; Faist, M. A.; Gong, W.; He, Z. C.; Wu, H. B.; Troughton, J.; Watson, T.; Bryant, D.; Nelson, J., Quantifying Losses in Open-Circuit Voltage in Solution-Processable Solar Cells, *Phys. Rev. Appl.*, **4**, 014020 (2015).
(30) Rand, B. P.; Burk, D. P.; Forrest, S. R., Offset energies at organic semiconductor heterojunctions and their influence on the open-circuit voltage of thin-film solar cells, *Phys. Rev. B*, **75**, 115327 (2007).
(31) Yang, L. Y.; Sinitsyn, N. A.; Chen, W. B.; Yuan, J. T.; Zhang, J.; Lou, J.; Crooker, S. A., Long-lived nanosecond spin relaxation and spin coherence of electrons in monolayer MoS_2 and WS_2, *Nat. Phys.*, **11**, 830-834 (2015).
(32) Wang, L.; Wu, M. W., Electron spin relaxation due to D'yakonov-Perel' and Elliot-Yafet mechanisms in monolayer MoS2: Role of intravalley and intervalley processes, *Phys. Rev. B*, **89**, 115302 (2014).
(33) Nienhaus, L.; Correa-Baena, J. P.; Wieghold, S.; Einzinger, M.; Lin, T. A.; Shulenberger, K. E.; Klein, N. D.; Wu, M. F.; Bulovic, V.; Buonassisi, T.; Baldo, M. A.; Bawendi, M. G., Triplet-Sensitization by Lead Halide Perovskite Thin Films for Near-Infrared-to- Visible Upconversion, *ACS Energy Lett.*, **4**, 888-895 (2019).
(34) Padilha, J. E.; Peelaers, H.; Janotti, A.; Van de Walle, C. G., Nature and evolution of the band-edge states in MoS2: From monolayer to bulk, *Phys. Rev. B*, **90**, 205420 (2014).
(35) Yeh, P. C.; Jin, W. C.; Zaki, N.; Zhang, D. T.; Liou, J. T.; Sadowski, J. T.; Al-Mahboob, A.; Dadap, J. I.; Herman, I. P.; Sutter, P.; Osgood, R. M., Layer-dependent electronic structure of an atomically heavy two-dimensional dichalcogenide, *Phys. Rev. B*, **91**, 041407 (2015).
(36) Mak, K. F.; Lee, C.; Hone, J.; Shan, J.; Heinz, T. F., Atomically Thin MoS2: A New Direct-Gap Semiconductor, *Phys. Rev. Lett.*, **105**, 136805 (2010).
(37) England, C. D.; Collins, G. E.; Schuerlein, T. J.; Armstrong, N. R., Epitaxial Thin-Films of Large Organic-Molecules - Characterization of Phthalocyanine and Coronene Overlayers on the Layered Semiconductors MoS_2 and SnS_2, *Langmuir*, **10**, 2748-2756 (1994).

(38) Chen, W.; Huang, H.; Chen, S.; Huang, Y. L.; Gao, X. Y.; Wee, A. T. S., Molecular Orientation-Dependent Ionization Potential of Organic Thin Films, *Chem. Mater.*, **20**, 7017-7021 (2008).
(39) Duhm, S.; Heimel, G.; Salzmann, I.; Glowatzki, H.; Johnson, R. L.; Vollmer, A.; Rabe, J. P.; Koch, N., Orientation-dependent ionization energies and interface dipoles in ordered molecular assemblies, *Nat. Mater.*, **7**, 326-332 (2008).
(40) Wang, T.; Chan, W. L., Dynamical Localization Limiting the Coherent Transport Range of Excitons in Organic Crystals, *J. Phys. Chem. Lett.*, **5**, 1812-1818 (2014).
(41) Yuan, H. T.; Liu, Z. K.; Xu, G.; Zhou, B.; Wu, S. F.; Dumcenco, D.; Yan, K.; Zhang, Y.; Mo, S. K.; Dudin, P.; Kandyba, V.; Yablonskikh, M.; Barinov, A.; Shen, Z. X.; Zhang, S. C.; Huang, Y. S.; Xu, X. D.; Hussain, Z.; Hwang, H. Y.; Cui, Y.; Chen, Y. L., Evolution of the Valley Position in Bulk Transition-Metal Chalcogenides and Their Monolayer Limit, *Nano Lett.*, **16**, 4738-4745 (2016).
(42) Zahid, F.; Liu, L.; Zhu, Y.; Wang, J.; Guo, H., A generic tight-binding model for monolayer, bilayer and bulk MoS_2, *AIP Adv.*, **3** (2013).
(43) Choi, J.; Zhang, H. Y.; Choi, J. H., Modulating Optoelectronic Properties of Two Dimensional Transition Metal Dichalcogenide Semiconductors by Photoinduced Charge Transfer, *ACS Nano*, **10**, 1671-1680 (2016).
(44) Liu, X. Y.; Xie, X. Y.; Fang, W. H.; Cui, G. L., Theoretical Insights into Interfacial Electron Transfer between Zinc Phthalocyanine and Molybdenum Disulfide, *J. Phys. Chem. A*, **122**, 9587-9596 (2018).
(45) Amsterdam, S. H.; Stanev, T. K.; Zhou, Q.; Lou, A. J. T.; Bergeron, H.; Darancet, P.; Hersam, M. C.; Stern, N. P.; Marks, T. J., Electronic Coupling in Metallophthalocyanine–Transition Metal Dichalcogenide Mixed-Dimensional Heterojunctions, *ACS Nano*, **13**, 4183-4190 (2019).
(46) England, C.; Collins, G.; Schuerlein, T.; Armstrong, N. R., Epitaxial thin films of large organic molecules: characterization of phthalocyanine and coronene overlayers on the layered semiconductors MoS_2 and SnS_2, *Langmuir*, **10**, 2748-2756 (1994).
(47) Wang, T.; Kafle, T. R.; Kattel, B.; Liu, Q. F.; Wu, J.; Chan, W. L., Growing Ultra-flat Organic Films on Graphene with a Face-on Stacking via Moderate Molecule-Substrate Interaction, *Sci. Rep.*, **6**, 28895 (2016).
(48) Oehzelt, M.; Akaike, K.; Koch, N.; Heimel, G., Energy-level alignment at organic heterointerfaces, *Sci. Adv.*, **1**, 1501127 (2015).
(49) Davidson, A. T., The Effect of the Metal Atom on the Absorption-Spectra of Phthalocyanine Films, *J. Chem. Phys.*, **77**, 168-172 (1982).
(50) Wang, T.; Liu, Q. F.; Caraiani, C.; Zhang, Y. P.; Wu, J.; Chan, W. L., Effect of Interlayer Coupling on Ultrafast Charge Transfer from Semiconducting Molecules to Mono- and Bilayer Graphene, *Phys. Rev. Appl.*, **4**, 014016 (2015).
(51) Wang, T.; Kafle, T. R.; Kattel, B.; Chan, W.-L., A Multidimensional View of Charge Transfer Excitons at Organic Donor–Acceptor Interfaces, *J. Am. Chem. Soc.*, **139**, 4098-4106 (2017).
(52) Jailaubekov, A. E.; Willard, A. P.; Tritsch, J. R.; Chan, W. L.; Sai, N.; Gearba, R.; Kaake, L. G.; Williams, K. J.; Leung, K.; Rossky, P. J.; Zhu, X. Y., Hot charge-transfer excitons set the time limit for charge separation at donor/acceptor interfaces in organic photovoltaics, *Nat. Mater.*, **12**, 66-73 (2013).
(53) Kafle, T. R.; Kattel, B.; Wang, T.; Chan, W.-L., The relationship between the coherent size, binding energy and dissociation dynamics of charge transfer excitons at organic interfaces, *J. Phys.: Condens. Matter*, **30**, 454001 (2018).

(54) Johannsen, J. C.; Ulstrup, S.; Cilento, F.; Crepaldi, A.; Zacchigna, M.; Cacho, C.; Turcu, I. C. E.; Springate, E.; Fromm, F.; Raidel, C.; Seyller, T.; Parmigiani, F.; Grioni, M.; Hofmann, P., Direct View of Hot Carrier Dynamics in Graphene, *Phys. Rev. Lett.*, **111**, 027403 (2013).
(55) Wallauer, R.; Reimann, J.; Armbrust, N.; Gudde, J.; Hofer, U., Intervalley scattering in MoS_2 imaged by two-photon photoemission with a high-harmonic probe, *Appl. Phys. Lett.*, **109**, 162102 (2016).
(56) Wang, T.; Kafle, T. R.; Kattel, B.; Chan, W. L., Observation of an Ultrafast Exciton Hopping Channel in Organic Semiconducting Crystals, *J. Phys. Chem. C*, **120**, 7491-7499 (2016).
(57) Norton, J. E.; Bredas, J. L., Theoretical characterization of titanyl phthalocyanine as a p-type organic semiconductor: Short intermolecular pi-pi interactions yield large electronic couplings and hole transport bandwidths, *J. Chem. Phys.*, **128**, 034701 (2008).
(58) Tant, J.; Geerts, Y. H.; Lehmann, M.; De Cupere, V.; Zucchi, G.; Laursen, B. W.; Bjornholm, T.; Lemaur, V.; Marcq, V.; Burquel, A.; Hennebicq, E.; Gardebien, F.; Viville, P.; Beljonne, D.; Lazzaroni, R.; Cornil, J., Liquid crystalline metal-free phthalocyanines designed for charge and exciton transport, *J. Phys. Chem. B*, **109**, 20315-20323 (2005).
(59) Jin, C. H.; Kim, J.; Utama, M. I. B.; Regan, E. C.; Kleemann, H.; Cai, H.; Shen, Y. X.; Shinner, M. J.; Sengupta, A.; Watanabe, K.; Taniguchi, T.; Tongay, S.; Zettl, A.; Wang, F., Imaging of pure spin-valley diffusion current in WS_2-WSe_2 heterostructures, *Science*, **360**, 893-896 (2018).
(60) Lim, H.; Kwon, H.; Kim, S. K.; Kim, J. W., Delayed Triplet-State Formation through Hybrid Charge Transfer Exciton at Copper Phthalocyanine/GaAs Heterojunction, *J. Phys. Chem. Lett.*, **8**, 4763-4768 (2017).
(61) Hufner, S. *Photoemission Spectroscopy: Principles and Applications*; Springer-Verlag: Berlin, 2003.
(62) Liu, H. L.; Shen, C. C.; Su, S. H.; Hsu, C. L.; Li, M. Y.; Li, L. J., Optical properties of monolayer transition metal dichalcogenides probed by spectroscopic ellipsometry, *Appl. Phys. Lett.*, **105**, 201905 (2014).
(63) Ceballos, F.; Bellus, M. Z.; Chiu, H. Y.; Zhao, H., Ultrafast Charge Separation and Indirect Exciton Formation in a MoS_2-$MoSe_2$ van der Waals Heterostructure, *ACS Nano*, **8**, 12717-12724 (2014).
(64) Peng, B.; Yu, G. N.; Liu, X. F.; Liu, B.; Liang, X.; Bi, L.; Deng, L. J.; Sum, T. C.; Loh, K. P., Ultrafast charge transfer in MoS_2/WSe_2 p-n Heterojunction, *2D Mater.*, **3**, 025020 (2016).
(65) Kattel, B.; Qin, L.; Kafle, T. R.; Chan, W. L., Graphene Field-Effect Transistor as a High-Throughput Platform to Probe Charge Separation at Donor-Acceptor Interfaces, *J. Phys. Chem. Lett.*, **9**, 1633-1641 (2018).
(66) Gregg, B. A., Entropy of Charge Separation in Organic Photovoltaic Cells: The Benefit of Higher Dimensionality, *J. Phys. Chem. Lett.*, **2**, 3013-3015 (2011).
(67) Clarke, T. M.; Durrant, J. R., Charge Photogeneration in Organic Solar Cells, *Chem. Rev.*, **110**, 6736-6767 (2010).
(68) Monahan, N. R.; Williams, K. W.; Kumar, B.; Nuckolls, C.; Zhu, X. Y., Direct Observation of Entropy-Driven Electron-Hole Pair Separation at an Organic Semiconductor Interface, *Phys. Rev. Lett.*, **114**, 247003 (2015).

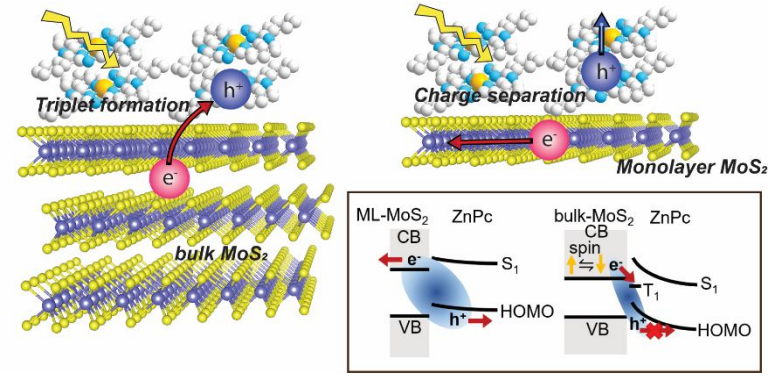
Triplet formation
h+
e-
bulk MoS2
Charge separation
h+
e-
Monolayer MoS2
ML-MoS2
ZnPc
CB
e-
S1
VB
h+
HOMO
bulk-MoS2
ZnPc
CB
spin
e-
T1
S1
VB
h+
HOMO

TOC figure

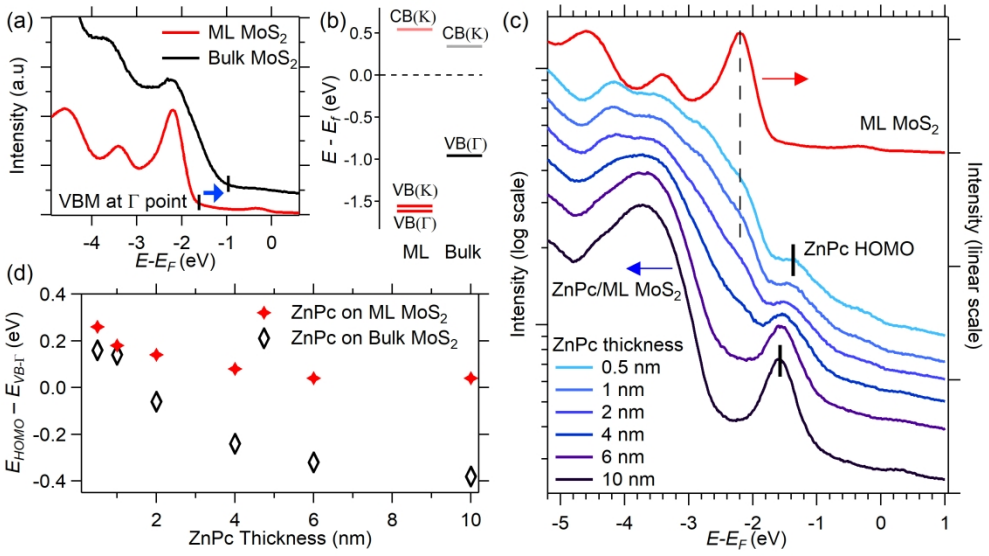
(a)
ML MoS2
Bulk MoS2
Intensity (a.u)
VBM at Γ point
E-EF (eV)
(b)
CB(K)
CB(K)
E - EF (eV)
VB(Γ)
VB(K)
VB(Γ)
ML Bulk
(c)
ML MoS2
ZnPc HOMO
ZnPc/ML MoS2
Intensity (log scale)
Intensity (linear scale)
ZnPc thickness
0.5 nm
1 nm
2 nm
4 nm
6 nm
10 nm
E-EF (eV)
(d)
ZnPc on ML MoS2
ZnPc on Bulk MoS2
EHOMO – EVB-Γ (eV)
ZnPc Thickness (nm)

Figure 1

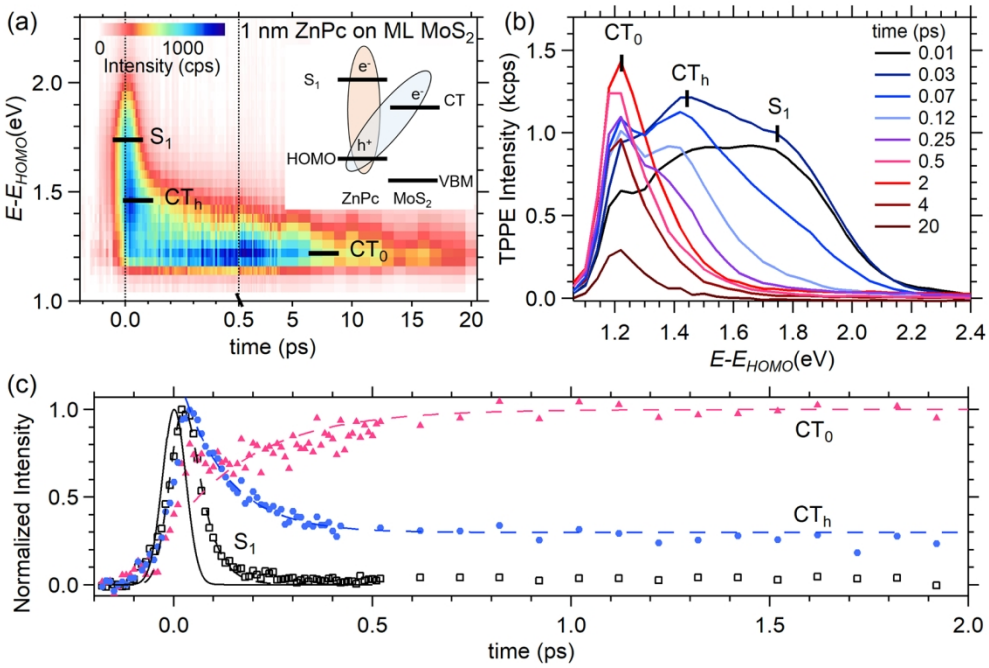
(a)
1 nm ZnPc on ML MoS2
0
1000
Intensity (cps)
S1
CTh
CT0
E-EHOMO(eV)
time (ps)
e-
S1
CT
h+
HOMO
VBM
ZnPc
MoS2
(b)
CT0
CTh
S1
time (ps)
0.01
0.03
0.07
0.12
0.25
0.5
2
4
20
TPPE Intensity (kcps)
E-EHOMO(eV)
(c)
CT0
CTh
S1
Normalized Intensity
time (ps)

Figure 2

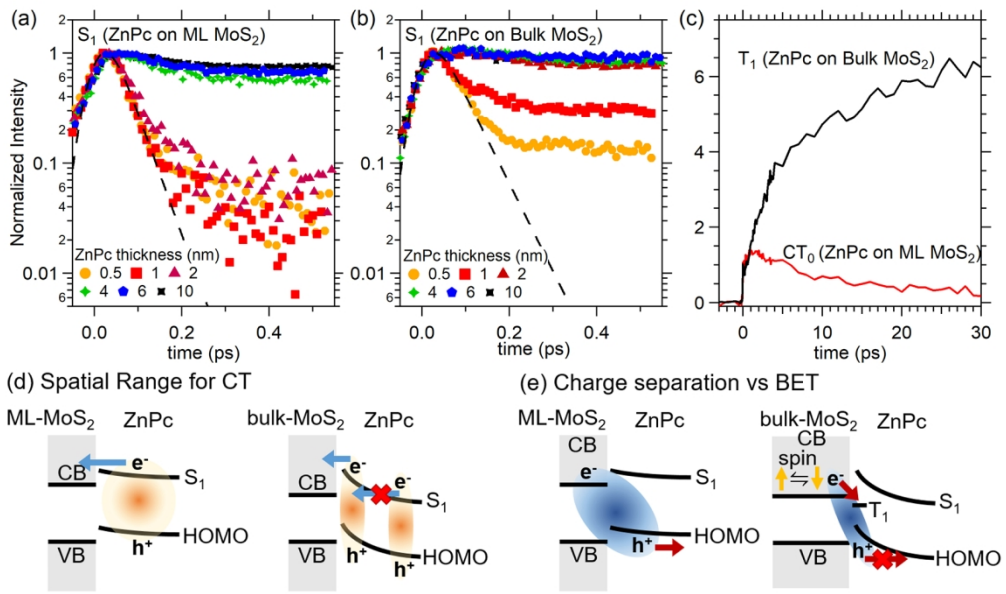
(a)
S1 (ZnPc on ML MoS2)
Normalized Intensity
ZnPc thickness (nm)
0.5 1 2
4 6 10
time (ps)
(b)
S1 (ZnPc on Bulk MoS2)
ZnPc thickness (nm)
0.5 1 2
4 6 10
time (ps)
(c)
T1 (ZnPc on Bulk MoS2)
CT0 (ZnPc on ML MoS2)
time (ps)
(d) Spatial Range for CT
ML-MoS2 ZnPc
CB
e-
S1
VB
h+
HOMO
bulk-MoS2 ZnPc
CB
e-
e-
S1
VB
h+
h+
HOMO
(e) Charge separation vs BET
ML-MoS2 ZnPc
CB
e-
S1
VB
h+
HOMO
bulk-MoS2 ZnPc
CB
spin
e-
T1
S1
VB
h+
HOMO

Figure 3

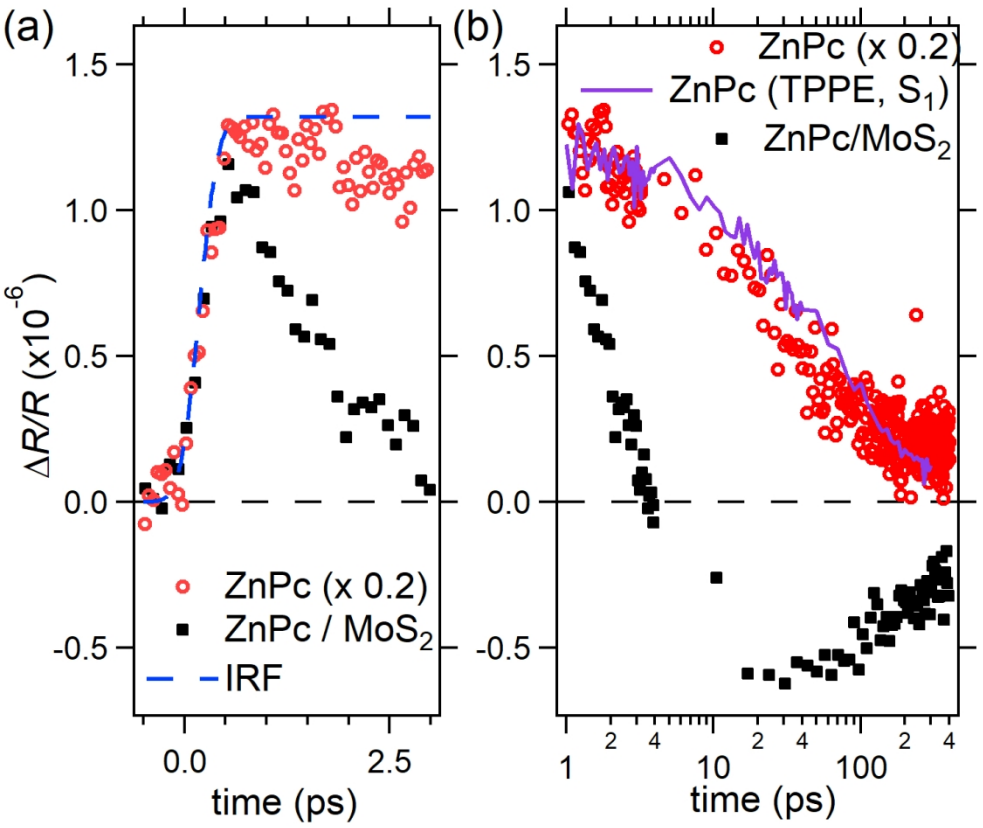
(a)
(b)
1.5
1.0
0.5
0.0
-0.5
ΔR/R (x10^-6)
ZnPc (x 0.2)
ZnPc / MoS2
IRF
0.0
2.5
time (ps)
ZnPc (x 0.2)
ZnPc (TPPE, S1)
ZnPc/MoS2
1
2
4
10
100
time (ps)

Figure 4

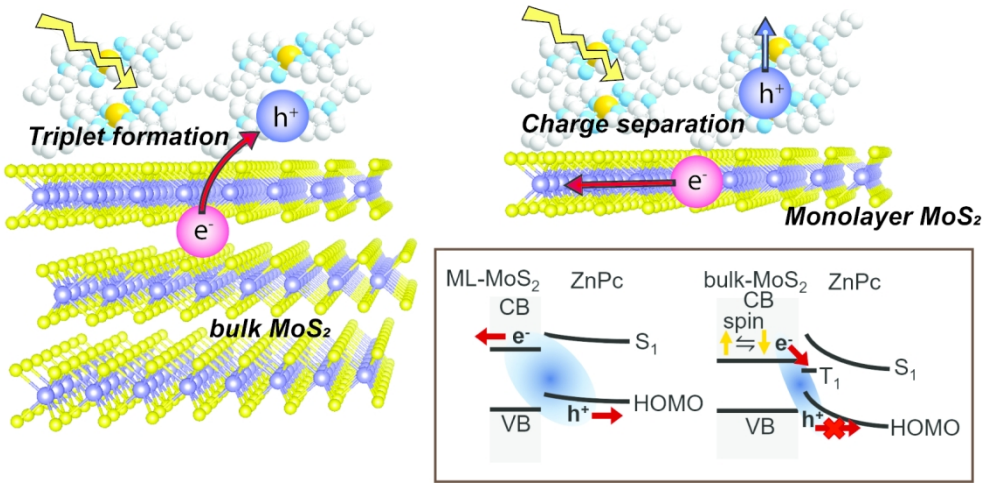
Triplet formation
h+
e-
bulk MoS2
Charge separation
h+
e-
Monolayer MoS2
ML-MoS2
ZnPc
CB
e-
S1
VB
h+
HOMO
bulk-MoS2
ZnPc
CB
spin
e-
T1
S1
VB
h+
HOMO

TOC figure